Chapter 4

Energy Bandgap Engineering of Transmission-Mode AlGaAs/GaAs Photocathode

Yijun Zhang and Gangcheng Jiao

Additional information is available at the end of the chapter

http://dx.doi.org/10.5772/intechopen.80704

Abstract

Aiming to enhance the photoemission capability in the waveband region of interest, a graded bandgap structure was applied to the conventional transmission-mode AlGaAs/GaAs photocathodes based on energy bandgap engineering, wherein the composition in $Al_xGa_{1-x}As$ window layer and the doping concentration in GaAs active layer were gradual. According to Spicer's three-step model, a photoemission theoretical model applicable to the novel transmission-mode $Al_xGa_{1-x}As$/GaAs photocathodes was deduced so as to guide the cathode structural design. Then the cathode material was grown by the metalorganic chemical vapor deposition technique, and the epitaxial cathode material quality was evaluated by the means of scanning electron microscope, electrochemical capacitance-voltage, X-ray diffraction and spectrophotometry. Through a series of specific processes, the cathode material was made into the multilayered module, possessing a glass/Si_3N_4/$Al_xGa_{1-x}As$/GaAs structure. After the surface treatment including heat cleaning and Cs—O activation for the cathode module, the image intensifier tube comprising the activated cathode module, microchannel plate, and phosphor screen was fabricated by indium sealing. The spectral response test results confirm the validity of the novel structure for the enhancement of blue-green photoresponse.

Keywords: AlGaAs/GaAs photocathode, graded bandgap, photoemission model, material epitaxy, tube fabrication

1. Introduction

Since negative-electron-affinity (NEA) GaAs photocathode was proposed as a type of excellent photoemitter by Scheer and Laar [1], GaAs-based photocathodes have found widespread applications in photodetectors, accelerators, electron microscopes, photon-enhanced thermionic emission devices, and other fields [2–5]. In view of the high visible spectral response,

good spectral extensibility to the near infrared (NIR) region and low dark current, NEA GaAs, GaAsP, and InGaAs photocathodes are important components in the vacuum photodetectors, for example, low-light-level (LLL) image intensifiers, photomultiplier tubes, and streak tubes [6]. In the modern light sources based on free electron lasers or energy recovery linacs, GaAs-based photocathodes serve as high brightness electron sources with the unique virtues of large current density driven by visible lasers, high spin polarization, low thermal emittance, and narrow energy distribution [7]. In recent years, a spin-polarized transmission electron microscope combining electron microscopy and accelerator technology using GaAs-GaAsP strained superlattice photocathodes was developed to observe dynamically a magnetic field images with high spatial and temporal resolutions [8]. Moreover, with the aid of the ultrahigh speed pulse laser, GaAs photocathodes can satisfy the requirements of fast response speed and large emission current density aiming to THz frequency vacuum devices [9].

As is well known, GaAs photocathodes can operate in the transmission-mode (t-mode) and the reflection-mode (r-mode), respectively, depending on the difference in the direction of the incident light [10, 11], as shown in **Figure 1**. For the t-mode operation, the incident light is irradiated on the substrate surface, and the photoelectrons are extracted from the opposite surface side, whereas for the r-mode operation, the incident light and photoelectrons are located on the same emission surface side. Due to the difference in absorption length of longwave and shortwave photons, the shapes of spectral response curves for GaAs photocathodes working in the two modes are different [11]. Differing from r-mode GaAs photocathodes, t-mode ones are difficult to achieve high spectral response in a broadband region from ultraviolet to NIR spectrum. Usually in the practical applications, the researches on t-mode photocathodes are more concerned. For example, the image intensifiers and related imaging systems, t-mode photocathodes conform to the optical imaging structure [12]. Besides, as polarized electron sources in photoinjector apparatus, t-mode photocathodes

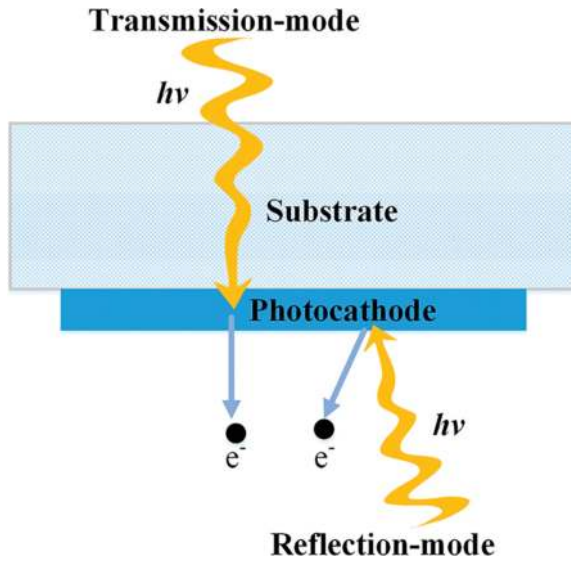

Figure 1. Schematic diagram of thin photocathode operating in the two different modes.

are more popular than r-mode ones, because the laser spot size can be reduced through the short focus lens placed on the photocathode backside, which would not hinder the path of the electron beam and is more conducive to achieve a super-high-brightness electron beam [13, 14].

As proposed by Spicer and Herreragomez [15], the photoemission process from photocathodes consists of electron excitation by incident light absorption, electron transport toward surface, and electron escape across the surface barrier into vacuum. For t-mode photocathodes, some important cathode parameters such as electron diffusion length, interface recombination velocity, and surface escape probability are crucial to the photoemission performance, especially the shortwave photosensitivity [16]. Enhancing the blue-green response of t-mode GaAs photocathodes as far as possible, would not only be beneficial to the detection in sandy or desert terrain for image intensifiers [17], but also increase the current density driven by 532 nm laser for electron sources [18]. Although the external electric field biased across the photocathodes can improve the photoemission capability, the limitations of this approach are the difficulty in making thin electrode pattern and the increased dark current with the strong field [19, 20]. In view of this adverse case, internal built-in electric fields through energy band engineering design could be an alternative approach. In our research, a complex structure composed of the composition-graded structure and the doping-graded structure is proposed to prepare high efficient t-mode AlGaAs/GaAs photocathodes. Furthermore, the photoemission model, cathode structure design, cathode material epitaxy, and vacuum tube fabrication are investigated through the integrated analysis of theory and experiments. Finally, the effectivity of the designed novel structure is verified by comparison with the common photocathodes.

2. Graded bandgap structure

For the t-mode GaAs photocathode, the AlGaAs and GaAs materials are usually used as the window layer and the active layer, which determine the shortwave cutoff and longwave cutoff, respectively. A built-in electric field in the interior of the photocathode material can be realized by the variation of dopant or composition according to energy band engineering design [21, 22]. Based on this concept, a novel structure is proposed to improve photoelectron emission capability, wherein a composition-graded structure and a doping-graded structure are employed to the $Al_xGa_{1-x}As$ window layer and GaAs active layer, respectively [23, 24], as shown in **Figure 2**. To form a built-in constant electrical field in the GaAs active layer of the photocathode, the p-type dopant concentration can follow the exponential variation, and the doping formula is expressed by [22]

$$N(y) = N_0 \exp(Ay) \tag{1}$$

where A denotes the exponential-doping (e-doping) factor, N_0 is the doping concentration at the surface of GaAs active layer, y is the distance from the coordinate origin (i.e., the surface of GaAs active layer), and $N(y)$ is the p-type doping concentration in the GaAs active layer. As a result of the variation of dopant concentration, the initial Fermi level is different. In thermal

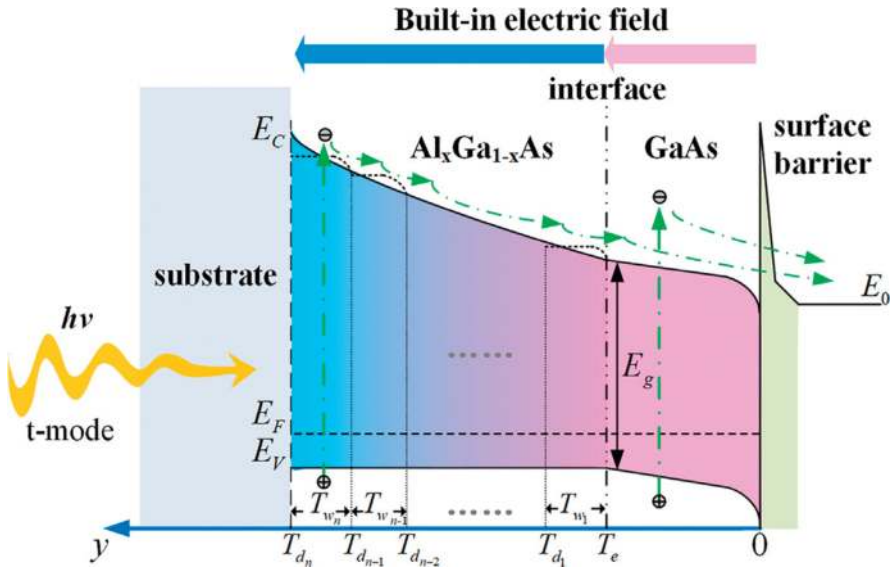

Figure 2. Energy band structure diagram of the t-mode $Al_xGa_{1-x}As$/GaAs photocathode with the graded bandgap structure. E_g is the bandgap, E_0 is the vacuum level, E_F is the Fermi level, E_C is the conduction band minimum, and E_V is the valence band maximum.

equilibrium, the Fermi level at different positions in the active layer is unified, and the electric potential energy $qV(y)$ is varied as follows:

$$qV(y) = k_B T \ln \frac{N(y)}{N_0} = k_B T A y \tag{2}$$

where q is the electron charge, T is the cathode temperature, and k_B is the Boltzmann constant. The diagram of band structure with the downward shape in the GaAs active layer is shown in **Figure 2**, wherein the built-in electric field E_0 in a certain thick (T_e) active layer is given by

$$E_0 = \frac{dV(y)}{dy} = \frac{k_B T A}{q} = \frac{k_B T}{q T_e} \ln \frac{N(y)|_{y=T_e}}{N_0} \tag{3}$$

In the $Al_xGa_{1-x}As$ window layer, the bandgap is decreased from the substrate interface to the GaAs interface due to the composition-graded structure. Because of the high p-type doping concentration, the valence bands of the $Al_xGa_{1-x}As$/GaAs heterojunction are aligned, as shown in **Figure 2**. The graded Al composition in the window layer results in a built-in electric field E_1, which is treated to be uniform as follows [25]:

$$E_1 = \frac{\Delta E_g}{q \Delta d} \tag{4}$$

where ΔE_g is the energy bandgap difference of $Al_xGa_{1-x}As$ material, and Δd is the overall thickness of $Al_xGa_{1-x}As$ window layer. **Figure 2** illustrates the transport process of photoexcited electrons in the t-mode graded bandgap $Al_xGa_{1-x}As$/GaAs photocathodes. As for the t-mode photocathodes, the photoelectrons generated by shortwave light excitation are

http://dx.doi.org/10.5772/intechopen.80704

distributed in the $Al_xGa_{1-x}As$ window layer. Under the first-stage built-in electric field, the thermalized photoelectrons in the $Al_xGa_{1-x}As$ layer move toward the GaAs interface. After that, the second-stage built-in electric field in the active layer can promote these photoelectrons toward the emission surface. On the other hand, the GaAs active layer can absorb the longwave light, and the excitated photoelectrons are promoted to move toward the surface with the help of the built-in electric field in the active layer. Consequently, there are reasons to believe that, by virtue of this unique graded bandgap structure, the quantum efficiency over the broadband spectrum, especially in the shortwave response region would be enhanced to some extent.

3. Photoemission model derivation and simulation

3.1. Photoemission model derivation

As is well known, the one-dimensional continuity equation can afford a useful avenue to establish the photoemission model of t-mode or r-mode III–V group photocathodes, which takes account of the spatial photon adsorption, spatial carrier distribution, and interface electron recombination [10, 11]. As shown in **Figure 2**, the photoelectrons generated in the $Al_xGa_{1-x}As$ layer are able to move into the GaAs layer and contribute to the total emitted electrons. For the composition-graded $Al_xGa_{1-x}As$ layer, some physical properties, for example, electron mobility (μ), electron diffusion coefficient (D_n), and electron recombination lifetime (τ) are the functions of the Al composition x, which are expressed as follows [26, 27]:

$$\mu = \begin{cases} 8000 - 22,000x + 10,000x^2 \ \left(\mathrm{cm}^2\ \mathrm{V}^{-1}\ \mathrm{S}^{-1}\right), & 0 < x < 0.45 \\ -255 + 1160x - 720x^2 \ \left(\mathrm{cm}^2\ \mathrm{V}^{-1}\ \mathrm{S}^{-1}\right), & 0.45 < x < 1 \end{cases} \tag{5}$$

$$D_n = \begin{cases} 200 - 550x + 250x^2 \ \left(\mathrm{cm}^2\ \mathrm{s}^{-1}\right), & 0 < x < 0.45 \\ -6.4 + 29x - 18x^2 \ \left(\mathrm{cm}^2\ \mathrm{s}^{-1}\right), & 0.45 < x < 1 \end{cases} \tag{6}$$

$$\tau = 29.142 + \frac{4.444 - 29.142}{1 + e^{\frac{x-0.3443}{0.00468}}}, \qquad 0 < \ x \ < 1 \tag{7}$$

Because of the aforesaid variable physical properties regarding to Al composition, the continuity equation of electron transport in the $Al_xGa_{1-x}As$ window layer is quite complex. For simplicity, the $Al_xGa_{1-x}As$ layer is treated to be of a series of sublayers with different Al compositions. As shown in **Figure 2**, the $Al_xGa_{1-x}As$ window layer can be considered to be of n sublayers, wherein T_{wn} denotes the thickness of nth sublayer, and T_{dn} denotes the coordinate point along the y-axis. In this case, the transport of photoelectrons in the $Al_xGa_{1-x}As$ window layer follows the one-dimensional continuity equation through diffusion and drift under the built-in electric field, which is as follows:

$$D_{ni}\frac{d^2n_i(y)}{dy^2} + \mu_i|E_1|\frac{dn_i(y)}{dy} - \frac{n_i(y)}{\tau_i} + g_i(y) = 0, \quad i = 1, 2, 3, \ldots\ldots, n \tag{8}$$

where $g_i(y)$ represents the photoelectron generation function in each $Al_xGa_{1-x}As$ sublayer and is expressed as [28, 29]:

$$g_i(y) = \begin{cases} (1-R_{hv})I_0\alpha_{hv_i}\left[\prod_{m=i+1}^{n}\exp\left(-\alpha_{hv_m}T_{w_m}\right)\right]\exp\left[-\alpha_{hv_i}\left(T_{d_i}-y\right)\right], & i=1,2,\ldots,n-1 \\ (1-R_{hv})I_0\alpha_{hv_i}\exp\left[-\alpha_{hv_i}\left(T_e+\sum_{i=1}^{n}T_{w_i}-y\right)\right], & i=n \end{cases} \tag{9}$$

In Eqs. (8) and (9), i represents the $Al_xGa_{1-x}As$ sublayer along the y axis direction, $n_i(y)$ and α_{hvi} denote the excess electron concentration and the absorption coefficient in each part of $Al_xGa_{1-x}As$ sublayer, I_0 is the incident light intensity, R_{hv} is the reflectivity at the light incident surface, and T_e is the active layer thickness. Besides, the three physical properties, that is, D_{ni}, μ_i, and τ_i in each sublayer are expressed by aforesaid Eqs. (5)–(7).

The excess electron concentration in the former sublayer should contribute to the latter sublayer, accordingly, the boundary conditions adequate for each sublayer are expressed as [28, 29]:

$$\begin{cases} \left[D_{ni}\dfrac{dn_i(y)}{dy}+\mu_i|E_1|n_i(y)\right]\Big|_{y=T_{d_i}} = -S_{v_{i+1}}n_i(y)\Big|_{y=T_{d_i}} + S_{v_{i+1}}n_{i+1}(y)\Big|_{y=T_{d_i}} \\ \left[D_{ni}\dfrac{dn_i(y)}{dy}+\mu_i|E_1|n_i(y)\right]\Big|_{y=T_e} = S_{vi}n_i(y)\Big|_{y=T_e} \end{cases}, \quad i=1 \tag{10}$$

$$\begin{cases} \left[D_{ni}\dfrac{dn_i(y)}{dy}+\mu_i|E_1|n_i(y)\right]\Big|_{y=T_{d_i}} = -S_{v_{i+1}}n_i(y)\Big|_{y=T_{d_i}} + S_{v_{i+1}}n_{i+1}(y)\Big|_{y=T_{d_i}} \\ \left[D_{ni}\dfrac{dn_i(y)}{dy}+\mu_i|E_1|n_i(y)\right]\Big|_{y=T_{d_{i-1}}} = S_{vi}n_i(y)\Big|_{y=T_{d_{i-1}}} \end{cases}, \quad i=2,\ldots,n-1 \tag{11}$$

$$\begin{cases} n_i(y)\Big|_{y=T_{d_i}} = 0 \\ \left[D_{ni}\dfrac{dn_i(y)}{dy}+\mu_i|E_1|n_i(y)\right]\Big|_{y=T_{d_{i-1}}} = S_{vi}n_i(y)\Big|_{y=T_{d_{i-1}}} \end{cases}, \quad i=n \tag{12}$$

where S_{vi} is the electron recombination velocity at each interface. By recursively solving the above continuity equations, the excess electron concentration $n_1(T_e)$ reaching the $Al_xGa_{1-x}As$/GaAs interface can be calculated.

As for the GaAs active layer, the excess electrons consist of electrons contributed from the $Al_xGa_{1-x}As$ window layer and electrons generated in the GaAs active layer. Under the second-stage built-in electric field, the photoelectron transport process in GaAs active layer follows the one-dimensional continuity equation as described by

$$D_{n0}\frac{d^2n_0(y)}{dy^2}+\mu_0|E_0|\frac{dn_0(y)}{dy}-\frac{n_0(y)}{\tau_0}+(1-R_{hv})I_0\alpha_{hv0}\left[\prod_{m=1}^{n}\exp\left(-\alpha_{hv_m}T_{w_m}\right)\right]\exp\left[-\alpha_{hv0}(T_e-y)\right]=0, \quad y\in[0,T_e] \tag{13}$$

where $n_0(y)$ is the excess electron concentration in the GaAs active layer, α_{hv0} is the absorption coefficient of the GaAs active layer, and D_{n0}, $\mu_{0,}$ and τ_0 denote the electron diffusion coefficient, the electron mobility, and the electron recombination lifetime in the GaAs active layer,

http://dx.doi.org/10.5772/intechopen.80704

respectively. Considering that the electrons from the $Al_xGa_{1-x}As$ window layer can contribute to the GaAs active layer, the boundary conditions adequate for Eq. (13) are given by [28]:

$$\left\{ \left[D_{n0} \frac{dn_0(y)}{dy} + \mu_0 |E_0| n_0(y) \right] \Big|_{y=T_e} = -S_{v1} n_0(y)\big|_{y=T_e} + S_{v1} n_1(y)\big|_{y=T_e} n_0(y)\big|_{y=0} = 0 \right. \tag{14}$$

By solving Eq. (13) via the boundary conditions Eq. (14) and the electron concentration $n_1(T_e)$ from the $Al_xGa_{1-x}As$ window layer, the concentration of electrons $n_0(y)$ in the active layer can be figured out. Finally, the quantum efficiency $Y(hv)$, defined as the emitted electron number per incident photon, for the complex $Al_xGa_{1-x}As$/GaAs photocathode is calculated as follows:

$$Y(hv) = PD_{n0} \frac{dn_0(y)}{dy} \Big|_{y=0} / I_0 \tag{15}$$

where P is the surface electron escape probability. If $E_0 = 0$, the quantum efficiency model of $Al_xGa_{1-x}As$/GaAs photocathode with the graded-composition (g-composition) and uniform-doping (u-doping) structure can be obtained. In the same way, when $E_1 = 0$ and $E_0 = 0$, we can also deduce the quantum efficiency model of common t-mode AlGaAs/GaAs photocathodes with the uniform-composition (u-composition) and u-doping structure. In a word, the aforementioned derivation method of photoemission model is applicable to those t-mode photocathodes with a common or complex structure.

Meanwhile, it is noted that the quantum efficiency has a close relation with the reflectivity $R(hv)$ of photocathode, as shown in Eqs. (9) and (13), thus the optical properties of t-mode graded bandgap $Al_xGa_{1-x}As$/GaAs photocathodes need to be investigated. In fact, the usual t-mode photocathode can be treated as a multilayer module, which comprises the glass faceplate, the antireflection layer, the window layer, and the GaAs active layer. The typical structure of t-mode $Al_xGa_{1-x}As$/GaAs photocathodes is shown in **Figure 3**. The glass substrate with a thickness of several millimeters is much thicker than other thin layers in the order of nanometers or micrometers, so the glass is treated as the incident medium rather than the thin film. The reflectivity of incident light permeating the glass substrate is greatly declined by the silicon nitride (Si_3N_4) antireflection film, and then the light in the wave range of interest is absorbed by the $Al_xGa_{1-x}As$ window layer and GaAs active layer in succession. The optical

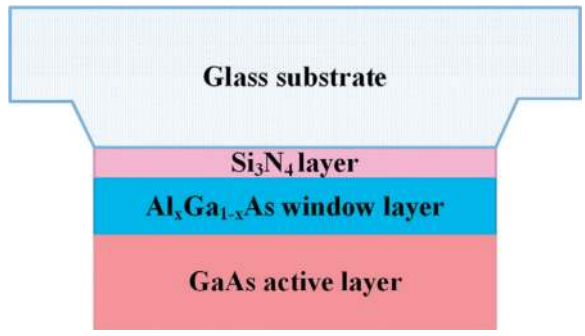

Figure 3. Structural schematic of multilayered t-mode GaAs cathode module, including the glass substrate, the Si_3N_4 antireflection layer, the $Al_xGa_{1-x}As$ window layer, and the GaAs active layer.

properties of multilayer module can be calculated based on the transfer matrix of thin-film optics, and the characteristic matrix of the multilayered cathode module is given by [30]:

$$\begin{bmatrix} B \\ C \end{bmatrix} = \left\{ \prod_{j=1}^{K} \begin{bmatrix} \cos\delta_j & \frac{\mathrm{i}}{\eta_j}\sin\delta_j \\ \mathrm{i}\eta_j \sin\delta_j & \cos\delta_j \end{bmatrix} \right\} \begin{bmatrix} 1 \\ \eta_{K+1} \end{bmatrix} \tag{16}$$

$$\delta_j = 2\pi\eta_j d_j \cos\theta_j/\lambda \tag{17}$$

$$\eta_j = n_j - ik_j \tag{18}$$

In Eqs. (16)–(18), δ_j and η_j are the optical phase difference and complex refractive index of the jth film layer, η_{K+1} is the optical constant of emergent medium, n_j and k_j constituting the complex refractive index are the refractivity and the extinction coefficient, d_j is the thickness of the jth film layer, and θ_j is the refraction angle of incident light. When light is perpendicularly incident on the surface of the glass substrate, the refraction angle is equal to zero. The reflectivity R_{hv} and transmittivity T_{hv} of the multilayered photocathode module can be calculated by the following expressions [30]

$$R_{hv} = \left(\frac{\eta_g B - C}{\eta_g B + C}\right)\left(\frac{\eta_g B - C}{\eta_g B + C}\right)^* \tag{19}$$

$$T_{hv} = \frac{4\eta_g \eta_{K+1}}{\left(\eta_g B + C\right)\left(\eta_g B + C\right)^*} \tag{20}$$

where η_g denotes the optical constant of the glass substrate. For the Al composition-varied window layer, the optical parameters, for example, the refractivity and extinction coefficient are different in each AlGaAs sublayer [31]. When the $Al_xGa_{1-x}As$ window layer is composed of n sublayers, the t-mode photocathode module can be treated as the thin film system of $n + 2$ layers to calculate the optical properties changing with incident photon wavelength, which are used as the necessary supplement to the quantum efficiency model.

3.2. Quantum efficiency simulation

As to the t-mode AlGaAs/GaAs photocathodes, the optical properties between the g-composition and u-composition structures should be different. For simplified calculation, the composition-graded $Al_xGa_{1-x}As$ window layer is assumed to be of five sublayers with the fixed Al composition in each sublayer. The five Al composition values are assumed to be 0.9, 0.675, 0.45, 0.225, and 0, respectively, distributed from the AlGaAs/Si_3N_4 interface to AlGaAs/GaAs interface. For the u-composition AlGaAs/GaAs photocathode, the Al composition in the AlGaAs window layer is assumed to be 0.7. The optical properties including the reflectivity R_{hv} and transmittivity T_{hv} can be simulated by utilizing Eqs. (16)–(20) by referring to the structure of **Figure 3**. In the simulations, the refractivity and extinction coefficients of $Al_xGa_{1-x}As$ with different Al compositions are referred to [31], the refractivity coefficients of glass and Si_3N_4 are

1.49 and 2.06, respectively, the extinction coefficients of glass and Si_3N_4 are zero due to no absorption, and the thicknesses of Si_3N_4, AlGaAs, and GaAs layer are assumed to be 100, 500 nm and 1.0 μm, respectively. Besides, each sublayer in the g-composition $Al_xGa_{1-x}As$ window layer is supposed to have the equal thickness of 0.1 μm. The simulated optical property curves between the two t-mode AlGaAs/GaAs photocathode modules with different window layer structures are shown in **Figure 4**. It is clear to see that the oscillation number in the entire 400–1100 nm region for the g-composition structure is less than those for the u-composition structure. In other words, compared with the u-composition $Al_{0.7}Ga_{0.3}As$/GaAs photocathode, the g-composition $Al_xGa_{1-x}As$/GaAs photocathode exhibits the much smoother reflectivity curve in the spectrum region of 400–900 nm, which is the concerned photon absorption waveband for the AlGaAs/GaAs material. Besides, in the 900–1100 nm region, the locations of peaks and valleys of the reflectivity curves for the g-composition $Al_xGa_{1-x}As$/GaAs photocathode move toward the shortwave direction, nevertheless, this has little effect on the photoemission performance of GaAs photocathodes since these photons with the wavelength greater than 900 nm are hardly absorbed by the GaAs material.

By using the deduced quantum efficiency models which take into account the reflectivity varying with the wavelength, the quantum efficiency curves of the t-mode $Al_xGa_{1-x}As$/GaAs photocathode with those unique graded bandgap structures are simulated, wherein the window layer is of the g- or u-composition structure, and the active layer is of the e- or u-doping structure, respectively. **Figure 5** exhibits the superiority of the $Al_xGa_{1-x}As$/GaAs photocathode with g-composition window layer and e-doping active layer. In **Figure 5**, some structural parameters such as the Al composition in the u-composition window layer, the Al composition

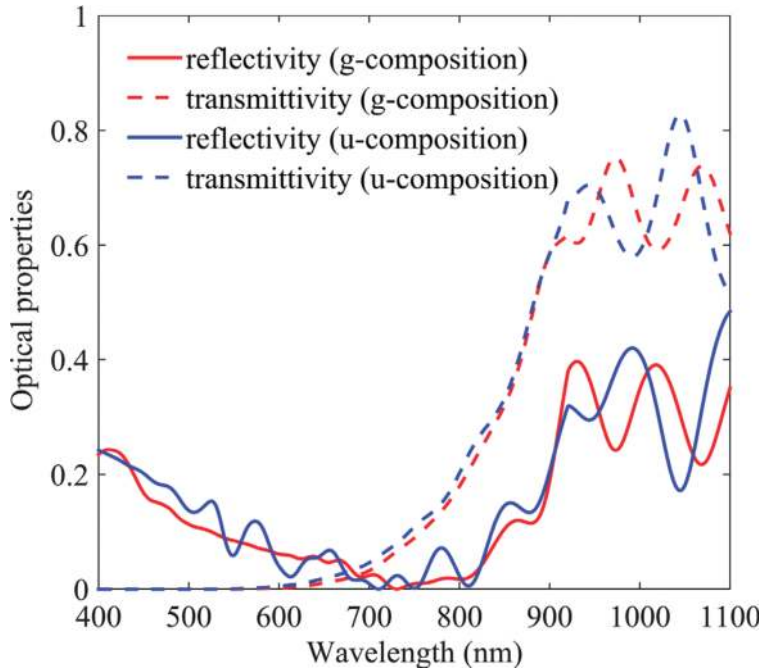

Figure 4. Simulation comparison of optical properties between the two cathode modules with different AlGaAs window layer structures.

distribution in each sublayer of $Al_xGa_{1-x}As$ window layer, and the thicknesses of Si_3N_4, AlGaAs and GaAs layers are identical to those in **Figure 4**. In the GaAs active layer, the doping concentration for e-doping structure is exponentially varied from 1×10^{19} to 1×10^{18} cm^{-3}, and that for the u-doping structure is 1×10^{19} cm^{-3}. In addition, the surface electron escape probability P is assumed to be 0.5. As a result of the reduced lattice mismatch by the seamless $Al_xGa_{1-x}As$/GaAs heterojunction, the interface recombination velocity S_{vi} for g-composition structure cannot exceed 10^4 cm/s, while S_v for the common u-composition structure is usually 10^6 cm/s [5].

It is seen clearly from **Figure 5** that the t-mode g-composition and e-doping photocathode can obtain the highest quantum efficiency in the spectrum region from 400 to 900 nm in contrast to other photocathodes. The quantum efficiency in the shortwave region, that is, blue-green region are enhanced greatly for the two former photocathodes with the g-composition structure. In the g-composition $Al_xGa_{1-x}As$ window layer, the photoelectrons excited by shortwave light would be promoted toward the GaAs active layer under the g-composition induced electric field. Then, these shortwave photoelectrons are successively boosted toward the emission surface under the built-in electric field formed by the e-doping structure. As shown in **Figure 5**, the e-doping structure for the g-composition $Al_xGa_{1-x}As$/GaAs photocathodes can slightly enhance the quantum efficiency, which is not like the case for the u-composition AlGaAs/GaAs photocathodes. The possible reason is that the g-composition $Al_xGa_{1-x}As$ layer can also absorb some extra longwave photons, which are originally absorbed by the GaAs active layer. In other words, more enough absorption space for longwave photons can be provided by the g-composition structure. While for the u-composition AlGaAs/GaAs

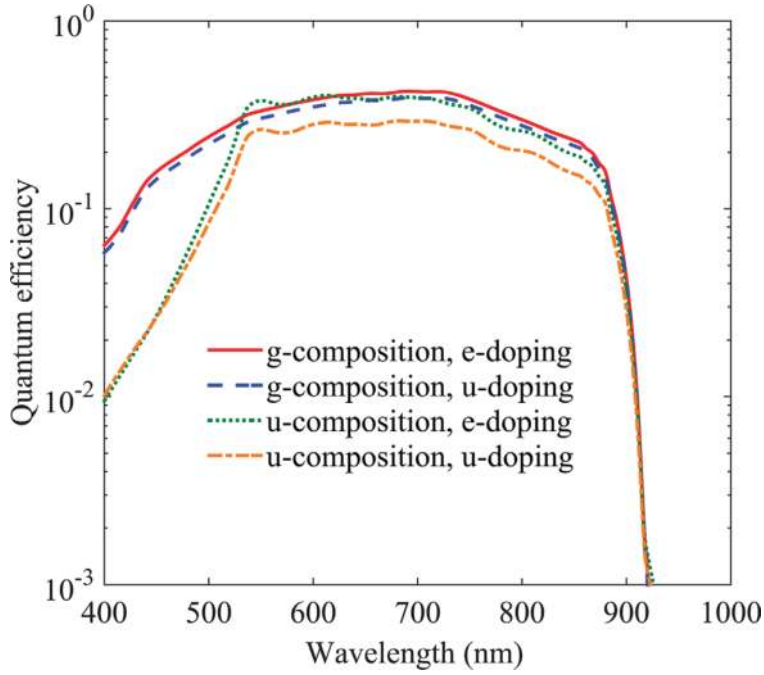

Figure 5. Simulation comparison of quantum efficiency among the t-mode photocathodes with different AlGaAs window layer and GaAs active layer structures.

http://dx.doi.org/10.5772/intechopen.80704

photocathodes, the case is different. The GaAs active layer just absorbs the longwave photons, and the transport efficiency for these generated photoelectrons can just be improved by the doping-induced electric field.

To guide the structural design of t-mode graded bandgap $Al_xGa_{1-x}As$/GaAs photocathode, the changes of quantum efficiency with the active layer thickness and the window layer thickness are analyzed, as shown in **Figure 6**. **Figure 6(a)** shows the changes of quantum efficiency curves with the active layer thickness T_e, assuming Al composition distribution, S_{vi} and T_{wi} are the same as those in **Figure 5**. As T_e increases, more space in the bulk for absorption of the longwave photons in the region of 650–900 nm is provided to generate more electrons to increase the quantum efficiency. If the GaAs active layer is thin, photoelectrons generated by shortwave light in the $Al_xGa_{1-x}As$ window layer would easily transport toward the GaAs active layer through diffusion and drift under the two-stage built-in electric field and finally escape into vacuum. In such a case, the quantum efficiency in the shortwave region would remain unchanged. Nevertheless, the thickness of the GaAs active layer must be controlled within a certain range, and the sufficiently thick active layer would decrease the quantum efficiency in the shortwave region, as shown in **Figure 6(a)**. Therefore, the thickness of the active layer should be designed to balance the longwave response and shortwave response. When the $Al_xGa_{1-x}As$ window layer is 500 nm in total thickness, the appropriate thickness is thought to be in the range of 1.0–1.5 μm.

Considering that the built-in electric field in the window layer is inversely proportional to window layer thickness, the effect of the window layer thickness on quantum efficiency in the shortwave region, especially in the blue-green waveband for g-composition photocathodes, is more pronounced than that for the u-composition ones. **Figure 6(b)** shows the quantum efficiency changing with the window layer thickness T_w, assuming T_e = 1.0 μm. As T_w decreases, the quantum efficiency in the waveband region from 400 to 720 nm is greatly enhanced arising from the enhanced g-composition induced electric field. When T_w is thin,

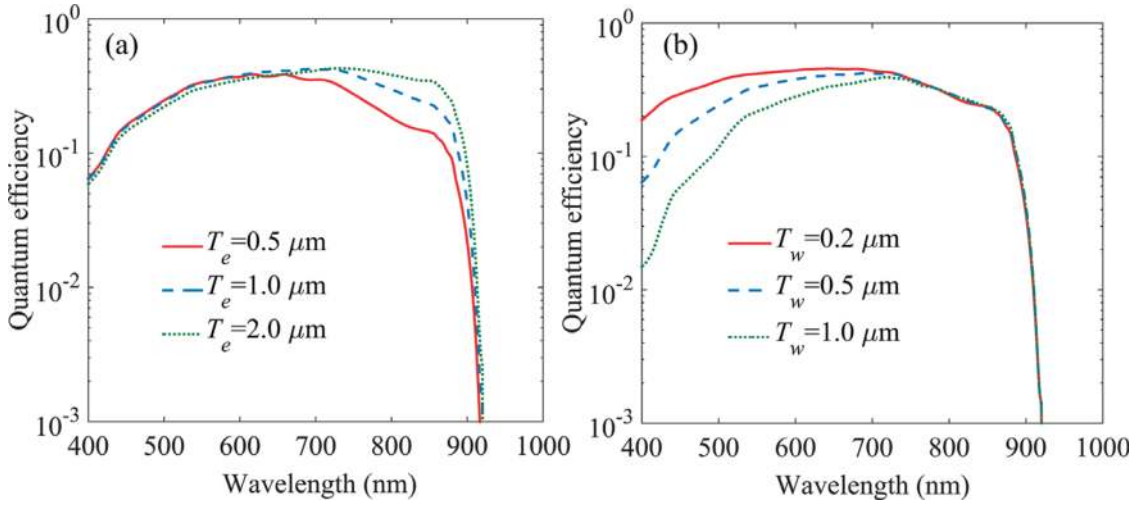

Figure 6. Quantum efficiency simulations with the changes of (a) active layer thickness and (b) window layer thickness for the t-mode graded bandgap $Al_xGa_{1-x}As$/GaAs photocathodes.

there is not enough space to absorb shortwave photons, and these shortwave photons can be absorbed by GaAs active layer. The quantum efficiency in the shortwave region would get increased as T_w decreases since that the transport capacity of photoelectrons in GaAs layer is better than that in AlGaAs layer. Nevertheless, a passivation layer is necessary to prevent impurities from the substrate into the active layer for the t-mode photocathodes, and thus the $Al_xGa_{1-x}As$ window layer also utilized as the passivation layer should not be extremely thin.

4. Epitaxial growth and quality characterization

4.1. Epitaxial growth of photocathode materials

In modern epitaxial growth techniques, the metalorganic chemical vapor deposition (MOCVD) technique is suitable for growing the complex ultrathin multilayer materials with the composition-graded or doping-graded structures. To confirm the actual effect of the g-composition and e-doping structure on the quantum efficiency of t-mode AlGaAs/GaAs photocathodes, the 2-inch-diameter $Al_xGa_{1-x}As$/GaAs epilayers with two different structures were grown on the low-defect n-type GaAs (100) substrates in the horizontal low-pressure MOCVD reactor from AIXTRON. As shown in **Figure 7(a)**, the multiple epitaxial layers consist of four AlGaAs/GaAs heterostructures, which follow the "inverted structure" technology [32, 33]. In **Figure 7(a)**, the AlGaAs stop layer serves as an etching-resistance layer, and the GaAs cap layer serves as an oxidation-blocking layer. The detailed structures of the two types of cathode materials are shown in **Figure 7(b)** and **(c)**. The difference between the two samples is the structure of window layer, wherein one is of g-composition $Al_xGa_{1-x}As$ layer, and the other is of u-composition $Al_{0.7}Ga_{0.3}As$ layer. Note that, as a result of the current epitaxial limitation, the GaAs active layer exhibits a quasi-exponential doping structure with the p-type dopant concentration varying from 1×10^{19} to 1×10^{18} cm^{-3}.

During the epitaxial growth process of the multiple layers, the group III sources are the trimethylgallium (TMGa) and trimethylaluminum (TMAl), the group V source was the AsH_3, the dopant source was the diethylzinc (DEZn), and the carrier gas was the H_2 gas. Additionally, the growth process was monitored in situ using the LayTech EpiRAS-200 spectrometer. The parameters of the epitaxial growth process are as follows: the growth rate was about 2.5 μm/h, the V/III flux ratio was adjusted at 10–15, the Al composition was controlled by the flow ratio of TMGa to TMAl, and the growth temperature was set as 680°C and 710°C for GaAs and $Al_xGa_{1-x}As$, respectively.

4.2. Quality characterization of photocathode materials

To understand the profile structure of the multilayered photocathode samples, the cross-sectional photographs of the multilayered structure for the two cathode material samples were measured by the scanning electron microscope (SEM) from Hitachi. It is clearly seen from **Figure 8** that differing from the case for u-composition sample, no sharp borderline exists at the interface of the $Al_xGa_{1-x}As$ window layer and GaAs active layer for the g-composition sample. This seamless interface would greatly reduce the interface electron recombination. It is

http://dx.doi.org/10.5772/intechopen.80704

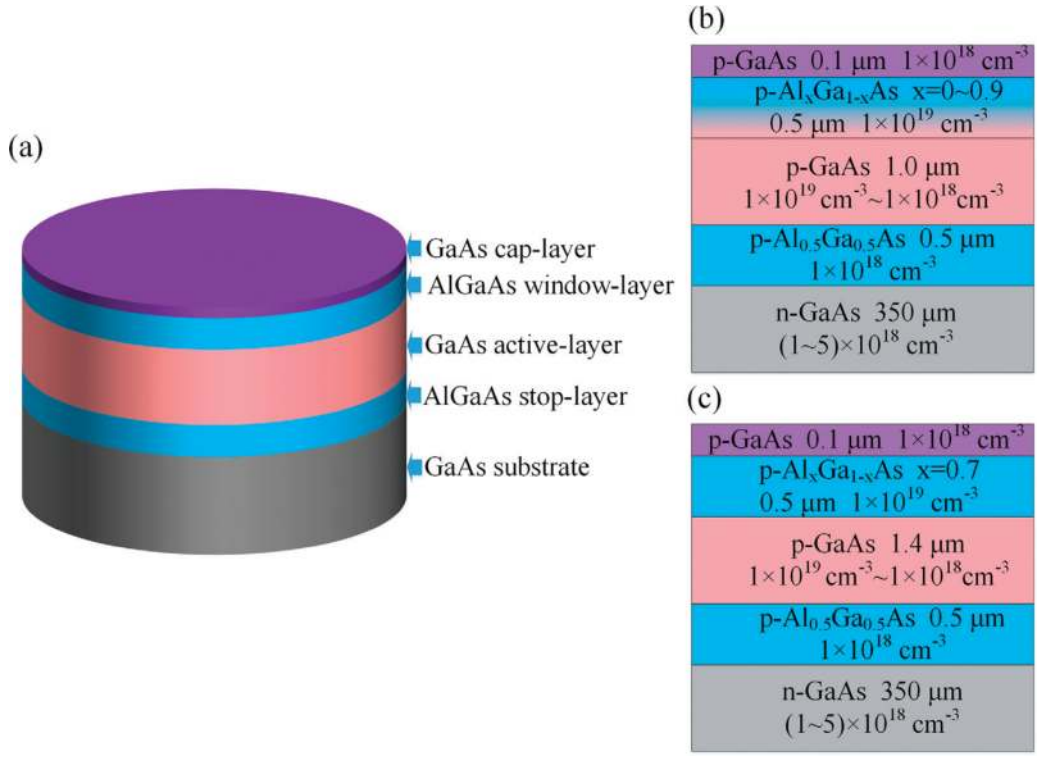

Figure 7. (a) Schematic diagram of the epitaxial t-mode AlGaAs/GaAs photocathode materials following the "inverted structure" technology, the detailed epitaxial structures of (b) g-composition and e-doping cathode sample, and (c) u-composition and e-doping cathode sample.

noted that many cracks in **Figure 8(b)** are caused by the inappropriate cleavage, which cannot reflect the true quality of the epitaxy. From the SEM photographs, it is judged that the vertically multilayered constructions of the epitaxial cathode materials agree well with the structural design.

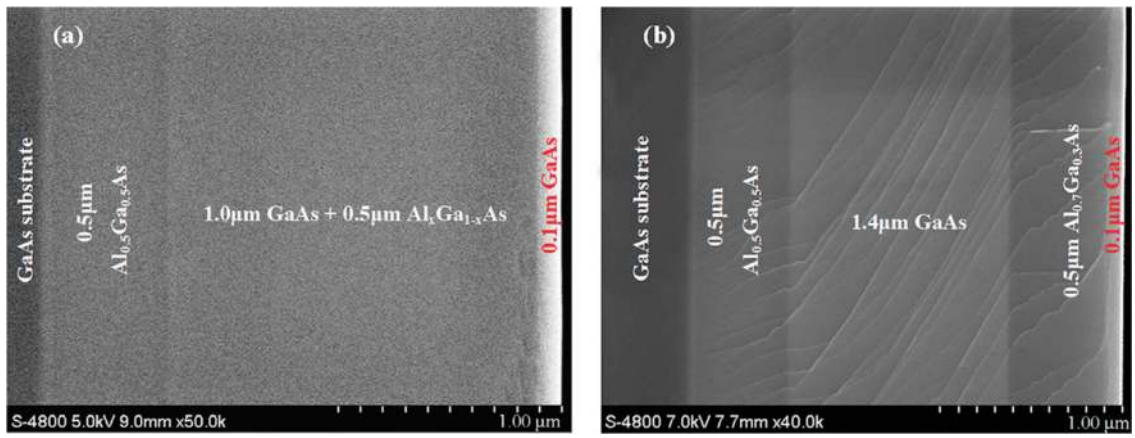

Figure 8. Cross-sectional SEM photographs of the cleaved epitaxial cathode samples with (a) g-composition and e-doping structure and (b) u-composition and e-doping structure.

The depth distribution of carrier concentration in the multilayered p-type AlGaAs/GaAs materials was measured by the electrochemical capacitance-voltage (ECV) system from Bio-Rad. As shown in **Figure 9**, a series of sublayers forming the graded doping structure can be realized by the MOCVD technique. The carrier concentration of no more than 8×10^{18} cm^{-3} in the GaAs active layer shows a gradient distribution. For the $Al_xGa_{1-x}As$ window layer in **Figure 9 (a)**, the carrier concentration decreases with the increase in Al composition, which exactly reflects the composition-graded structure.

To investigate the crystalline quality of the epitaxial cathode materials, the X-ray diffraction (XRD) curves were measured by the X'Pert Pro MRD system. As shown in **Figure 10**, the

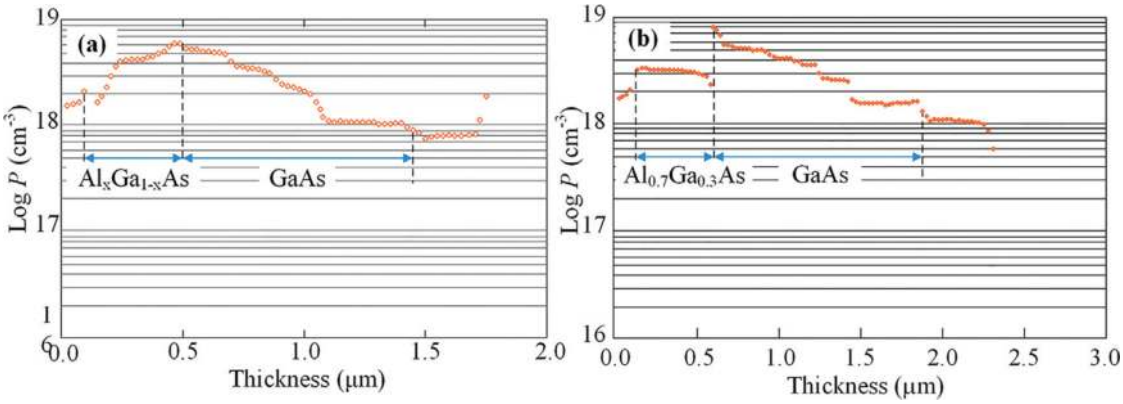

Figure 9. Depth distribution of carrier concentration in the cleaved epitaxial cathode samples with (a) g-composition and e-doping structure and (b) u-composition and e-doping structure.

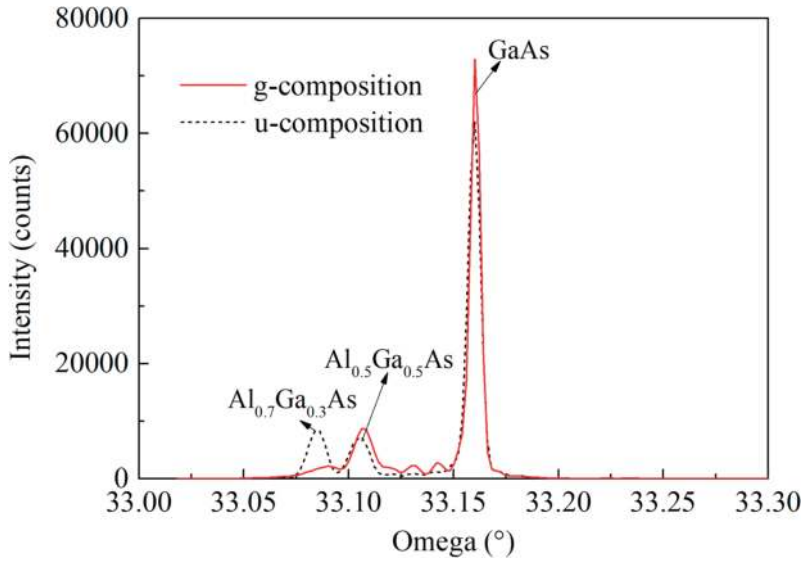

Figure 10. XRD curves of the cleaved epitaxial cathode samples with two different structures.

rightmost peak represents the GaAs material, which is the superposition of the diffraction peaks of the GaAs cap layer, active layer, and substrate. The only one diffraction peak indicates that the crystalline perfection of the GaAs epilayers is consistent with the GaAs substrate. The left two diffraction peaks for the u-composition sample represent the AlGaAs window layer and stop layer, respectively. In the g-composition sample, there is no diffraction peak denoting the window layer, and a series of diffraction peaks exist nearby the peak of the GaAs layer, which are caused by the g-composition $Al_xGa_{1-x}As$ epilayer. The slightly narrower full width at half maximum of the GaAs diffraction peak indicates that the GaAs active layer in the g-composition sample has a better crystalline quality.

5. Device fabrication and spectral response

5.1. Transmission-mode cathode module fabrication

Following the recipe of fabricating glass-sealed t-mode AlGaAs/GaAs photocathodes [32, 33], the epitaxial cathode materials cutted from the 2-inch-diameter epitaxial wafer were fabricated into the multilayered t-mode cathode module. The schematic process flow for fabricating t-mode AlGaAs/GaAs photocathode modules is shown in **Figure 11**. First, the GaAs cap layer was removed by chemical etching to expose the AlGaAs window layer, and by plasma enhanced chemical vapor deposition (PECVD), a thin antireflective layer of 100 nm-thick Si_3N_4 was deposited on the exposed window layer surface. Then, the 7056 glass, serving as the incident window and support layer, was bonded on the Si_3N_4 antireflection layer by thermocompression. Following that, through selective etching process, the GaAs substrate and AlGaAs stop layer were etched away to expose the GaAs active layer to prepare the NEA surface [32]. Finally, the Cr-Ni ring electrode applied to bias on the cathode was prepared by the physical vapor deposition (PVD), such as magnetron sputtering method. After these processing steps, the multilayered cathode module with a glass/Si_3N_4/AlGaAs/GaAs structure was finished. In addition, to eliminate etching-induced damage at the active layer surface, the polishing treatment was implemented, which slightly decreased the thickness of the GaAs active layer.

The optical property curves of the t-mode cathode modules with two different structures were measured by utilizing the Shimadzu UV-3600 spectrophotometer, which possesses three detectors working from ultraviolet to NIR waveband. The optical properties were measured based on the double optical path method, and light was incident on the surface of glass faceplate in a normal direction. **Figure 12** shows the experimental reflectivity and transmissivity curves of the two different multilayered module samples. It is found that, just as the simulated results in **Figure 4**, the reflectivity curve in the region of 400–800 nm for g-composition structure is relatively smoother than that for u-composition structure. In other words, the smooth reflectivity curve verifies the composition-graded structure in the $Al_xGa_{1-x}As$ window layer from another aspect. Thereby, the characterization results regarding the cross-sectional photographs, carrier concentration distributions, X-ray diffraction peaks, and optical properties all reflect the special design structure.

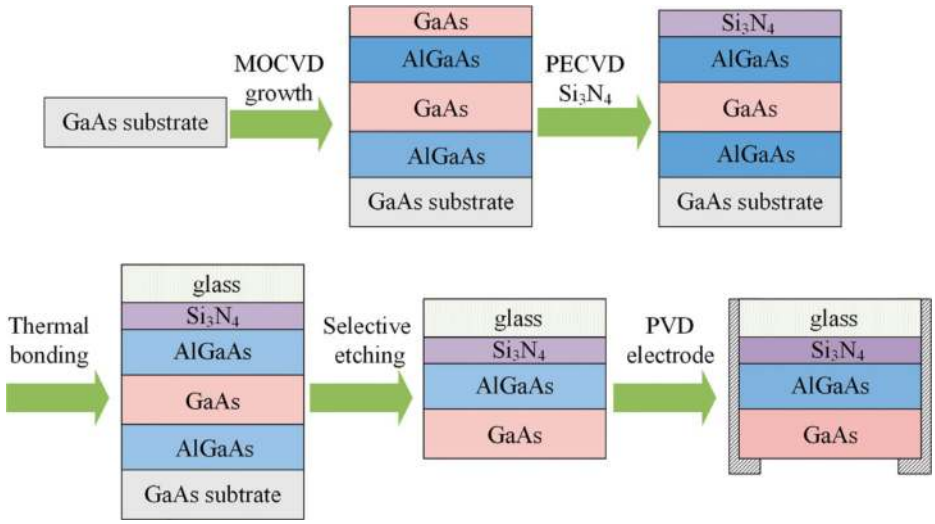

Figure 11. Schematic of the process flow for fabricating t-mode AlGaAs/GaAs photocathode modules following the "inverted structure" technology.

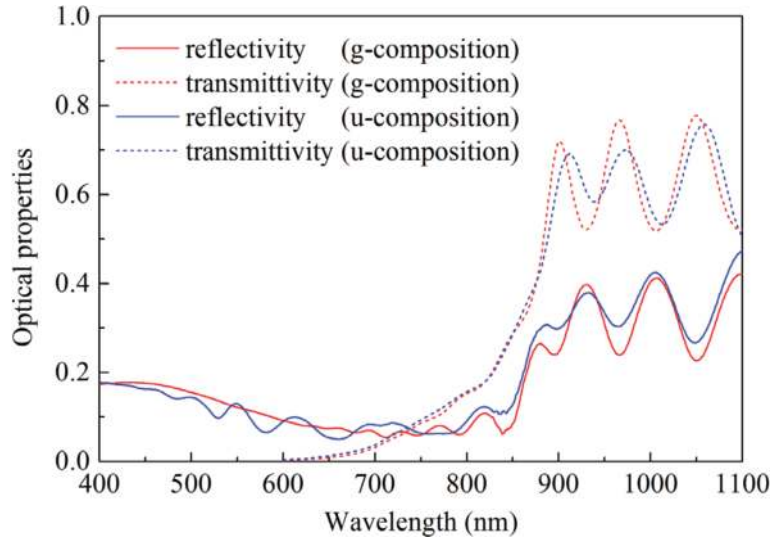

Figure 12. Experimental optical property curves of the t-mode AlGaAs/GaAs cathode modules with two different structures.

5.2. Activation of photocathode surface

Prior to activation, the 18-mm-diameter cathode modules experienced the chemical cleaning and vacuum annealing to obtain an atomic level clean surface. The heat treatment with a suitable temperature under ultrahigh vacuum (UHV) condition is particularly important for the activation, and the quadrupole mass spectrometer (QMS) was adopted to monitor the change of residual gas components during the programmed temperature rose and fell. **Figure 13** shows the changes of mainly concerned residual gas components for the two t-mode cathode module

samples. Through detecting the gas presence of the QMS traces at m/e = 18 (H_2O), 75 (As), 91 (AsO), 150 (As_2), and 156 (Ga_2O), it can be judged that whether the oxides on the GaAs surface, such as As_2O_3 and Ga_2O_3, are cleared away with the increased temperature or not [34]. It can be inferred from **Figure 13** that both the cathode module samples obtained an oxide-free clean surface after the heat treatment procedure in terms of these obvious QMS trace peaks.

After the sample cooled to room temperature, the Cs—O activation to form the NEA state at the cathode surface was performed in the UHV chamber with a base pressure of 10^{-9} Pa. The Cs and O sources used in the activation are solid dispensers easily controlled by direct current, and the flux is proportional to the operating current [35]. During the activation, the Cs source was on all the time, and the O source was switched on and off [35]. The operating current of Cs and O dispensers was regulated by program control current supply, and the photocurrent induced by a white light source was monitored in real time by the computer-controlled test system [35]. The initial Cs supply caused the gradual increase of the photocurrent. With the continuous Cs flux, when the photocurrent dropped to 80% of its peak, the O source was open. In subsequent alternate activation cycles, the O source was closed when the photocurrent reached its peak and was open again when the photocurrent dropped to 80% of the peak. The operating current ratio of Cs source to O source for both samples was regulated as the same 1.65/1.8. Until the photocurrent peak no longer increased, the O source and Cs source were closed successively, and the activation process was finished. To further improve the photoemission performance, the second heat treatment with a lower temperature was employed to the samples [36]. After that, the samples were activated again using the same co-deposition activation. As seen from **Figure 14**, the second activation can dramatically enhance the final cathode performance. Meanwhile, the final photocurrent peaks of the two samples are approximately the same.

5.3. Tube package and spectral response test

After the two-step Cs—O activation process, the cathode module in the UHV activation chamber was transferred to the UHV seal vacuum chamber and indium sealed into an image

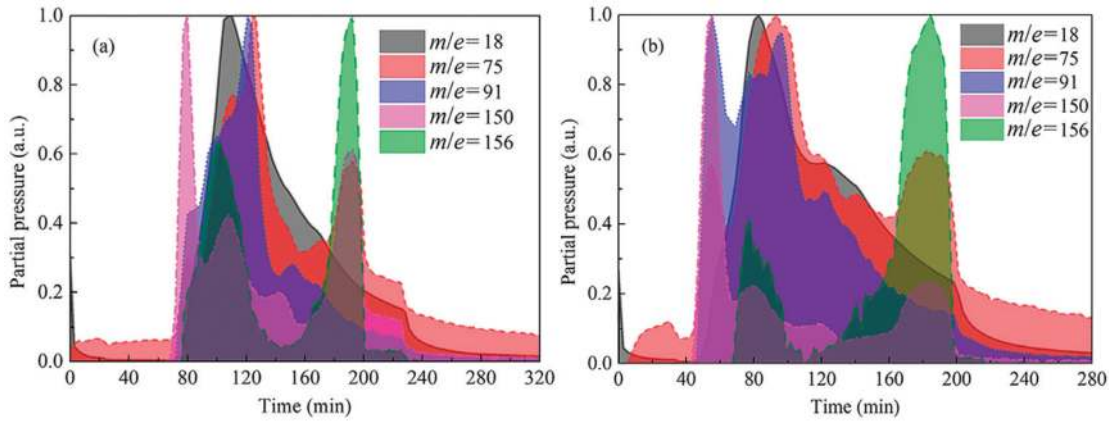

Figure 13. Residual gas changes during high-temperature thermal cleaning process for (a) g-composition and (b) u-composition AlGaAs/GaAs cathode modules.

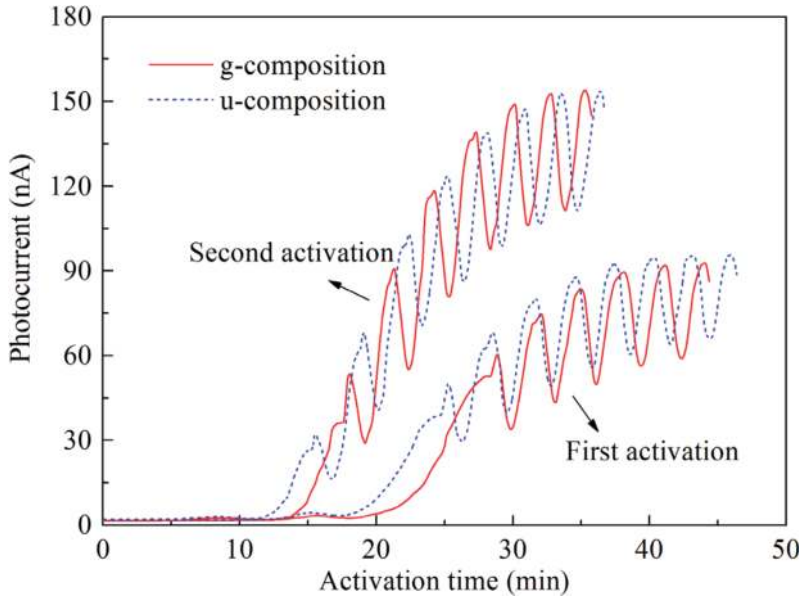

Figure 14. Photocurrent changes during Cs—O activation for the two t-mode AlGaAs/GaAs cathode modules.

intensifier tube, wherein the t-mode AlGaAs/GaAs cathode module was equipped in association with the filmed microchannel plate (MCP), phosphor screen, output window, ceramics, and Kovar sealing parts [37]. The schematic structure and the photograph of the LLL proximity focused image intensifier are shown in **Figure 15**. As shown in **Figure 15(a)**, the proximity focused image intensifier is capable of enhancing a LLL image from several thousands to tens of thousands of times. The input LLL image is converted into photoelectrons by the AlGaAs/GaAs photocathode, and then the number of photoelectrons is multiplied several thousands of times by the MCP coated with a thin ion barrier film which can prevent ion feedback. Lastly, the multiplied photoelectrons bombard the phosphor screen and are converted into photons.

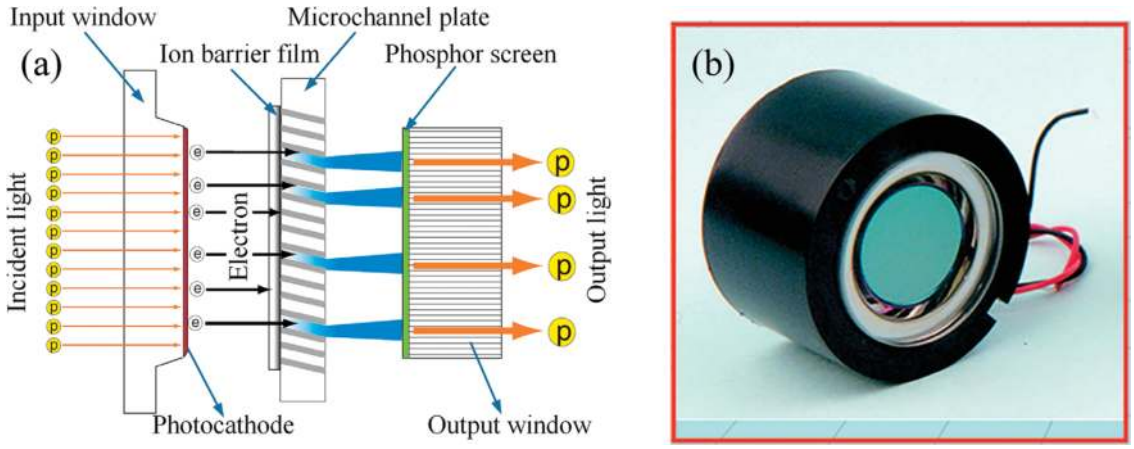

Figure 15. (a) Schematic structure of the low-light-level proximity focused image intensifier and (b) photograph of the sealed proximity focused image intensifier.

http://dx.doi.org/10.5772/intechopen.80704

Thus, the input LLL image is intensified and appears as the output image on the phosphor screen. In addition to the function of direct eye observation, the LLL image intensifier can be coupled with CCD/CMOS array by the fiber optic taper to realize video output and remote monitoring [38, 39].

The sealed image intensifiers were extracted from the seal vacuum chamber into ambient air, and the spectral response curves were measured by the spectral response testing instrument [22]. Through the spectral response values corresponding to the wavelength, the quantum efficiency values corresponding to the wavelength for the two different cathode samples were obtained [40]. In the spectral region of 600–750 nm, the quantum efficiency exceeds 40%. As shown in **Figure 16**, it is found that in contrast to the u-composition structure, the g-composition structure is especially useful to the enhancement of shortwave quantum efficiency, which conforms to the original intention of our design concept. By fitting the experimental optical property and quantum efficiency data based on the theoretical photoemission model, the internal cathode parameters difficult to be measured directly can be obtained. The thickness values of each layer calculated by fitting the experimental reflectivity and transmittivity curves are listed in **Table 1**. It is seen that the Al composition in the g-composition window layer is not distributed uniformly, and the sublayers with low Al composition are relatively thinner compared to those with high Al composition. For the two samples, the thicknesses of the GaAs active layer are smaller than the design values, which are caused by the polishing treatment after the fabrication of cathode modules.

By means of fitting the experimental quantum efficiency curves, we can obtain some performance parameters, for example, interface recombination velocity S_v and surface escape probability P. It is seen from **Table 1** that the two samples have the same P, which means that the

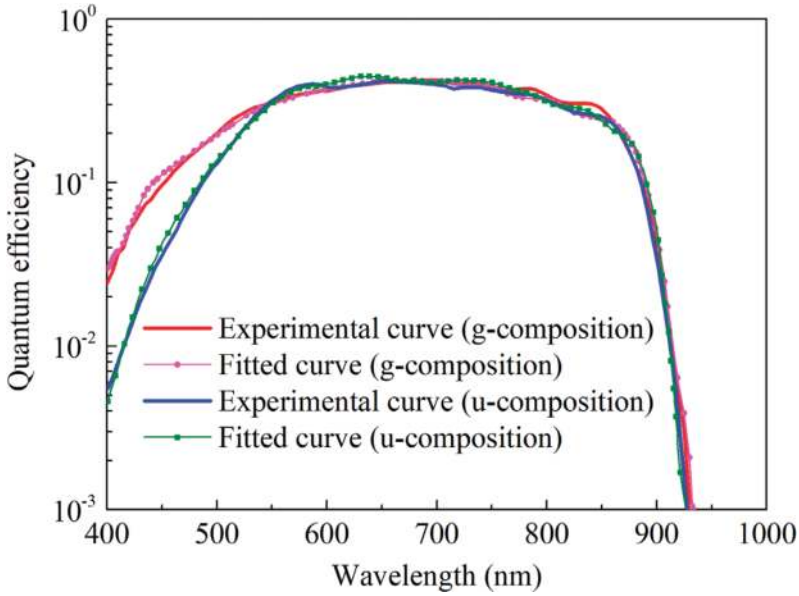

Figure 16. Experimental and fitted quantum efficiency curves for the two different t-mode AlGaAs/GaAs photocathodes samples.

Cathode sample	d_{Si3N4} (nm)	Al composition in each AlGaAs sublayer	d_{AlGaAs} (nm)	d_{GaAs} (nm)	S_v (cm/s)	P
g-Composition	109	0.9	106	857	10^3	0.52
		0.675	117			
		0.45	125			
		0.225	63			
		0	72			
u-Composition	107	0.7	485	1256	10^5	0.52

Table 1. Fitted parameters of the two different t-mode AlGaAs/GaAs photocathode samples.

surface barrier shapes changed by the activation process are the same. Whereas, S_v for the g-composition sample, it is considerably reduced in contrast to that for the u-composition sample. It is known that the S_v is mainly determined by the crystal quality of photocathode itself, such as misfit dislocations and stacking faults at the AlGaAs/GaAs interface. The g-composition structure in the window layer can not only mitigate the interface discontinuity caused by the interface lattice mismatch, but also form an internal electric field to facilitate the transport of shortwave photons excited electrons toward the emitting surface.

6. Conclusions

In this chapter, we have carried out systematically theoretical and experimental researches on t-mode AlGaAs/GaAs photocathodes, with regard to bandgap structure design, photoemission model derivation, epitaxial growth, surface activation, device fabrication, and performance evaluation. Compared with the common t-mode AlGaAs/GaAs photocathode, the graded bandgap t-mode $Al_xGa_{1-x}As$/GaAs photocathode with a g-composition and e-doping structure can achieve higher quantum efficiency in the shortwave response region, particularly the blue-green spectral region of interest. In addition, this g-composition structure is helpful to mitigate the interface recombination and enhance the absorption of the longwave light, which leads to the enhanced photoemission capability. This work has reference significance for the design of other graded bandgap III-V group photocathodes.

Acknowledgements

This work was supported by the National Natural Science Foundation of China (grant nos. 61771245 and 61301023) and Science and Technology on Low-Light-Level Night Vision Laboratory Foundation of China (grant no. J20150702). The authors would like to thank Dr. Feng Cheng for her efforts in the theoretical photoemission model, and the staff from Science and Technology on Low-Light-Level Night Vision Laboratory for their assistance in the fabrication of t-mode cathode modules and image intensifiers.

Author details

Yijun Zhang[1]* and Gangcheng Jiao[2]

*Address all correspondence to: zhangyijun423@njust.edu.cn

1 School of Electronic and Optical Engineering, Nanjing University of Science and Technology, Nanjing, China

2 Science and Technology on Low-Light-Level Night Vision Laboratory, Xi'an, China

References

[1] Scheer JJ, Laar JV. GaAs-Cs: A new type of photoemitter. Solid State Communications. 1965;**3**:189-193

[2] Chrzanowski K. Review of night vision technology. Opto-Electronics Review. 2013;**21**:153-181

[3] Liu W, Chen Y, Lu W, Moy A, Poelker M, Stutzman M, et al. Record-level quantum efficiency from a high polarization strained GaAs/GaAsP superlattice photocathode with distributed Bragg reflector. Applied Physics Letters. 2016;**109**:252104

[4] Baum A, Arcuni P, Aebi V, Presley S, Elder M. Prototype negative electron affinity-based multibeam electron gun for lithography and microscopy. Journal of Vacuum Science and Technology B. 1999;**17**:2819-2822

[5] Schwede JW, Sarmiento T, Narasimhan VK, Rosenthal SJ, Riley DC, Schmitt F, et al. Photon-enhanced thermionic emission from heterostructures with low interface recombination. Nature Communications. 2013;**4**:1576

[6] Williams BF, Tietjen JJ. Current status of negative electron affinity devices. Proceedings of the IEEE. 1971;**59**:1489-1497

[7] Karkare S, Boulet L, Cultrera L, Dunham B, Liu X, Schaff W, et al. Ultrabright and ultrafast III–V semiconductor photocathodes. Physical Review Letters. 2014;**112**:097601

[8] Kuwahara M, Takeda Y, Saitoh K, Ujihara T, Asano H, Nakanishi T, et al. Development of spin-polarized transmission electron microscope. Journal of Physics: Conference Series. 2011;**298**:012016

[9] Mitsuno K, Masuzawa T, Hatanaka Y, Neo Y, Mimura H. Activation process of GaAs NEA photocathode and its spectral sensitivity. In: 3rd International Conference on Nanotechnologies and Biomedical Engineering. Singapore: Springer; 2016. pp. 163-166

[10] Martinelli RU, Fisher DG. The application of semiconductors with negative electron affinity surfaces to electron emission devices. Proceedings of the IEEE. 1974;**62**:1339-1360

[11] Antypas GA, James LW, Uebbing JJ. Operation of III-V semiconductor photocathodes in the semitransparent mode. Journal of Applied Physics. 1970;**41**:2888-2894

[12] Estrera JP, Ostromek T, Bacarella A, Isbell W, Iosue MJ, Saldana M, et al. Advanced image intensifier night vision system technologies: Status and summary 2002. Proceedings of SPIE. 2003;**4796**:49-59

[13] Jin X, Yamamoto N, Nakagawa Y, Mano A, Kato T, Tanioku M, et al. Super-high brightness and high-spin-polarization photocathode. Applied Physics Express. 2008;**1**:045002

[14] Pastuszka S, Hoppe M, Kratzmann D, Schwalm D, Wolf A, Jaroshevich AS, et al. Preparation and performance of transmission-mode GaAs photocathodes as sources for cold dc electron beams. Journal of Applied Physics. 2000;**88**:6788-6800

[15] Spicer WE, Herreragomez A. Modern theory and applications of photocathodes. Proceedings of SPIE. 1993;**2022**:18-35

[16] Fisher DG, Enstrom RE, Escher JS, Gossenberger HF, Appert JR. Photoemission characteristics of transmission-mode negative electron affinity GaAs and (ln,Ga)As vapor-grown structures. IEEE Transactions on Electron Devices. 1974;**21**:641-649

[17] Sinor TW, Estrera JP, Phillips DL, Rector MK. Extended blue GaAs image intensifiers. Proceedings of SPIE. 1995;**2551**:130-134

[18] Zhang S, Benson SV, H-Garcia C. Observation and measurement of temperature rise and distribution on GaAs photo-cathode wafer with a 532 nm drive laser and a thermal imaging camera. Nuclear Instruments and Methods in Physics Research. 2011;**631**:22-25

[19] Spicer WE. Negative affinity 3-5 photocathodes: Their physics and technology. Applied Physics. 1977;**12**:115-130

[20] Costello K, Aebi V, Davis G, Rue RL, Weiss R. Transferred electron photocathode with greater than 20% quantum efficiency beyond 1 micron. Proceedings of SPIE. 1995;**2550**: 177-188

[21] Jones LB, Rozhkov SA, Bakin VV, Kosolobov SN, Militsyn BL, Scheibler HE, et al. Cooled transmission-mode NEA-photocathode with a band-graded active layer for high brightness electron source. AIP Conference Proceedings. 2008;**1149**:1057-1061

[22] Zhang YJ, Niu J, Zhao J, Chang BK, Shi F, Cheng HC. Influence of exponential-doping structure on photoemission capability of transmission-mode GaAs photocathodes. Journal of Applied Physics. 2010;**108**:093108

[23] Zhang YJ, Chang BK, Niu J, Zhao J, Zou JJ, Shi F, et al. High-efficiency graded band-gap $Al_xGa_{1-x}As$/GaAs photocathodes grown by metalorganic chemical vapor deposition. Applied Physics Letters. 2011;**99**:101104

[24] Feng C, Zhang YJ, Qian Y, Chang BK, Shi F, Jiao GC, et al. Photoemission from advanced heterostructured $Al_xGa_{1-x}As$/GaAs photocathodes under multilevel built-in electric field. Optics Express. 2015;**23**:19478-19488

[25] Yang Y, Yang W, Sun C. Heterostructured cathode with graded bandgap window-layer for photon-enhanced thermionic emission solar energy converters. Solar Energy Materials & Solar Cells. 2015;**132**:410-417

[26] Levinshtein M, Shur MS, Rumyanstev S, editors. Handbook Series on Semiconductor Parameters. Vol. 2. London: World Scientific; 1999

[27] Zarem HA, Lebens JA, Nordstrom KB, Sercel PC, Sanders S, Eng LE, et al. Effect of Al mole fraction on carrier diffusion lengths and lifetimes in $Al_xGa_{1-x}As$. Applied Physics Letters. 1989;**55**:2622-2624

[28] Feng C, Zhang YJ, Qian YS, Xu Y, Liu XX, Jiao GC. Quantum efficiency of transmission-mode $Al_xGa_{1-x}As$/GaAs photocathodes with graded-composition and exponential-doping structure. Optics Communications. 2016;**369**:50-55

[29] Feng C, Zhang YJ, Qian YS, Wang ZH, Liu J, Chang BK, et al. High-efficiency $Al_xGa_{1-x}As$/GaAs cathode for photon-enhanced thermionic emission solar energy converters. Optics Communications. 2018;**413**:1-7

[30] Zhao J, Xiong YJ, Chang BK, Zhang YJ, Zhang JJ. Research on optical properties of transmission-mode GaAs photocathode module. Proceedings of SPIE. 2011;**8194**:81940J

[31] Aspnes DE, Kelso SM, Logan RA, Bhat R. Optical properties of $Al_xGa_{1-x}As$. Journal of Applied Physics. 1986;**60**:754-767

[32] Antypas GA, Edgecumbe J. Glass-sealed GaAs-AlGaAs transmission photocathode. Applied Physics Letters. 1975;**26**:371-372

[33] André JP, Guittard P, Hallais J, Piaget C. GaAs photocathodes for low light level imaging. Journal of Crystal Growth. 1981;**55**:235-245

[34] Yamada M, Ide Y. Anomalous behaviors observed in the isothermal desorption of GaAs surface oxides. Surface Science. 1995;**339**:L914-L918

[35] Zhang YJ, Qian YS, Feng C, Shi F, Cheng HC, Zou JJ, et al. Improved activation technique for preparing high-efficiency GaAs photocathodes. Optical Materials Express. 2017;**7**:3456

[36] Rodway DC, Allenson MB. In situ surface study of the activating layer on GaAs (Cs, O) photocathodes. Journal of Physics D: Applied Physics. 1986;**19**:1353-1371

[37] Thomas N. System performance advances of 18-mm and 16-mm subminiature image intensifier sensors. Proceedings of SPIE. 2000;**4128**:54-64

[38] Nützel G. Single-photon imaging using electron multiplication in vacuum. In: Seitz P, Theuwissen AJP, editors. Single-Photon Imaging. Berlin: Springer; 2011. pp. 73-102

[39] Vallerga JV, Siegmund O, Dalcomo J, Jelinsky PN. High-resolution (<10 μm) photon-counting intensified CCD. Proceedings of SPIE. 1997;**3019**:156-167

[40] Zhang YJ, Zou JJ, Niu J, Chang BK, Xiong YJ. Variation of spectral response for exponential-doped transmission-mode GaAs photocathodes in the preparation process. Applied Optics. 2010;**49**:3935-3940